The Structure and Predictability of the "High-Latitude Mode" in the CSIRO9 General Circulation Model

JOHN W. KIDSON

National Institute of Water and Atmospheric Research Ltd., Wellington, New Zealand

IAN G. WATTERSON

CSIRO Division of Atmospheric Research and Cooperative Research Centre for Southern Hemisphere Meteorology, Melbourne, Australia

(Manuscript received 2 February 1998, in final form 26 January 1999)

ABSTRACT

The CSIRO9 general circulation model shows a zonally symmetric mode of variability, which closely resembles the high-latitude mode (HLM) in middle and high latitudes of the Southern Hemisphere. The leading EOF of the zonal mean zonal wind between 30° and 68°S, whose amplitude has been taken as an index of the HLM, shows opposing variations centered near 40° and 60°S accounting for 43% of the daily variance. Analysis has concentrated on composites for periods when the index changed quickly between significant peaks of the opposite sign or persisted with a large amplitude for an extended period. The momentum flux variations are small at the northern and southern boundaries and the principal variations are centered near 49°S between the maxima in the zonal wind. The changes in angular momentum content are around 30% smaller in the southern band. Eddy heat fluxes are less coherent but help in maintaining the zonal wind anomalies against friction.

A simple model of the zonal wind index with stochastic forcing and linear damping reproduces its short period variations well but is less successful in simulating the observed continuity over 10- to 20-day lags.

1. Introduction

The "high-latitude mode" (HLM) is a consistent feature of low-frequency variations in the Southern Hemisphere circulation. It has an equivalent barotropic structure with a high degree of zonal symmetry and is observable both as a reversal in phase in tropospheric height fields near 60°S (Rogers and van Loon 1982; Kidson 1988b, 1991; Nigam 1990), and an alternation in zonal wind strength between latitudes near 40° and 60°S (Trenberth 1979; Karoly 1990; Kidson 1988a). The amplitude and location of the opposing wind maxima show little variation with the season and are largely independent of the seasonal variation in the polar and subtropical jets (Hartmann and Lo 1998).

By convention, an index representing the shear between the opposing zonal wind anomalies takes the sign of the zonal wind anomaly near 60°S. When this index is positive, the polar vortex is constricted and the polar jet is strong. A subtropical jet may also be present in the Australia–New Zealand sector, particularly during winter and spring (Kidson and Sinclair 1995). In the low index phase, meridional cross sections show a broad zonal wind maximum at midlatitudes. Although it is largely a zonally symmetric pattern, the high-latitude vortex is displaced so that it is centered around the Antarctic continent rather than the pole. At midlatitudes there are generally signs of a 3–4 wave pattern (e.g., Kidson 1988b). The changes in the jet location and strength throughout the cycle are also reflected in cyclone activity, which is displaced southward when index values are high (Sinclair et al. 1997). The peak amplitude of the eddy momentum flux shows little variation with the phase of the HLM but its location is displaced over a range of about 10° latitude (Kidson and Sinclair 1995). The role of heat fluxes appears to be relatively small although fluxes contribute to the maintenance of anomalous mean flow against friction (Karoly 1990).

A similar oscillation also appears in a number of numerical models, ranging from the simple two-level model of Robinson and Qin (1992) to more complex multilevel simulations (e.g., Zwiers 1987; Yu and Hartmann 1993). The extensive analysis of Yu and Hartmann (1993), and later of Hartmann (1995), has clarified the role of momentum fluxes and the advection of potential vorticity in helping to develop and maintain the extreme phases of the oscillation. Recent modeling studies have

Corresponding author address: Dr. John W. Kidson, NIWA, P.O. Box 14-901, Wellington, New Zealand.
E-mail: j.kidson@niwa.cri.nz

concentrated on the role of the eddy heat and momentum fluxes driving the zonal wind variations (Robinson 1994, 1996; Feldstein 1995, 1998; Lee and Feldstein 1996; James and Dodd 1996; Hartmann and Lo 1998). These point to a stochastic origin for the eddy forcing but differ on the extent of the feedback from the zonal flow to the eddies. Akahori and Yoden (1997) and Hartmann and Zuercher (1998) have linked extreme departures in the position of the zonal jet to alternative cyclonic and anticyclonic wave-breaking regimes whose establishment may be critically dependent on the barotropic shear.

In addition to its theoretical interest, the HLM is one of the few consistent low-frequency phenomena affecting Southern Hemisphere weather and a greater knowledge of its behavior might potentially improve monthly and seasonal forecasting. In this context it would be useful to find what triggers a change in phase of the HLM, whether situations can be identified where it is unusually persistent, and whether there are times when the mode is more or less predictable.

While it would be desirable to examine these questions using observed data (e.g., Hartmann and Lo 1998; Feldstein 1998), even the new reanalysis datasets (Kalnay et al. 1996) suffer to some extent from inadequate data coverage over the oceanic regions of the Southern Hemisphere. We have chosen instead to examine the output of the CSIRO9 model, which is one of the better-performing GCMs for the Southern Hemisphere and has a good representation of the split jet in the Australasian region (Mullan and McAvaney 1995). As with other models, the data are complete, dynamically consistent, and avoid the discontinuities associated with the assimilation of daily data. We have taken advantage of the 8-h time period between archived data fields to show more clearly the time evolution of the zonal index and associated variables.

While this study was originally motivated by a desire to improve local climate forecasts, it is of interest to compare the behavior of the HLM within this model with that found in previous observational and modeling studies. Some of its general characteristics are reviewed in section 2, and more detailed analyses of composites for transitional periods and persistent spells are presented in section 3. In section 4 we describe attempts to reproduce the observed behavior of the HLM index in terms of a simple stochastic model with linear damping, and conclusions are presented in section 5.

2. General properties of HLM in the CSIRO9 GCM

The CSIRO9 general circulation model (Watterson et al. 1997) has nine vertical sigma levels and an R21 spectral representation. It includes a semi-Lagrangian treatment of water vapor transport, dynamic sea ice, and a bare soil and canopy land surface scheme, as well as standard parameterizations of radiation, cloud, precipitation, atmospheric turbulence, and the surface boundary layer. Four options are available for dealing with the sea surface: ''S,'' SST specified from a climatological annual cycle; ''G,'' SST and ice cover specified from observations; ''M,'' SST calculated from a mixed-layer heat equation; and ''C,'' SST determined by a fully coupled ocean GCM.

While interaction with the sea surface appears to play a small role in increasing the persistence of the high-latitude mode on longer timescales (Watterson 2000), the HLM shows generally similar properties in all four versions of the model. Our analysis is based on a 30-yr simulation from version M for which a complete set of output fields is available at 8-h intervals.

a. Derivation of the HLM index

In order to facilitate further analysis, an index was defined that would represent the state of reversal in zonal wind strength between middle and higher latitudes. The derivation of this index made use of the zonal mean winds at the 0.5-σ ($\sim$500 hPa) level in the model. As the mode extends throughout the troposphere with a barotropic structure (Fig. 2), similar results would be expected for any level near the maximum amplitude in the middle and upper troposphere. Although the zonal wind shear between 60° and 40°S would serve quite well as an index, we chose to apply EOF analysis to the departures of the zonal mean zonal winds from their mean annual cycle (e.g., Kidson 1988a and other previous references). The annual cycle for each latitude was obtained by applying a 1:2:1 smoother to the 30-yr daily mean values. The initial analysis covered the zonal means between 21° and 72°S and showed the leading mode to have variations in the opposite phase in broad bands centered near 40° and 60°S and contained within the overall limits of 30.3°–68.5°S. The HLM index was defined by the component scores of the leading EOF, which contributed 43.2% of the variance in this more limited latitude range. Its structure is shown in Fig. 1 along with the other significant EOFS, 2 and 3, which, respectively, contribute 30.4% and 12.9% of the variance. Positive index values correspond to stronger zonal winds at high latitudes, in keeping with the usual convention. Hartmann and Lo's (1998) analysis suggests that similar results would have been obtained for EOF 1, but with the patterns displaced to the north, if we had used angular momentum anomalies rather than the zonal wind.

b. Basic relationships with the HLM index

The correlations of the time series of the HLM index with the zonal mean zonal wind $[u]$, eddy momentum flux $[u^*v^*]$, temperature $[T]$, and heat flux $[v^*T^*]$ anomalies are shown in Fig. 2. (Note that $[\,\cdot\,]$ indicates zonal average and ''*'' a deviation from it.) The pattern for $[u]$ agrees well with those found in the observational

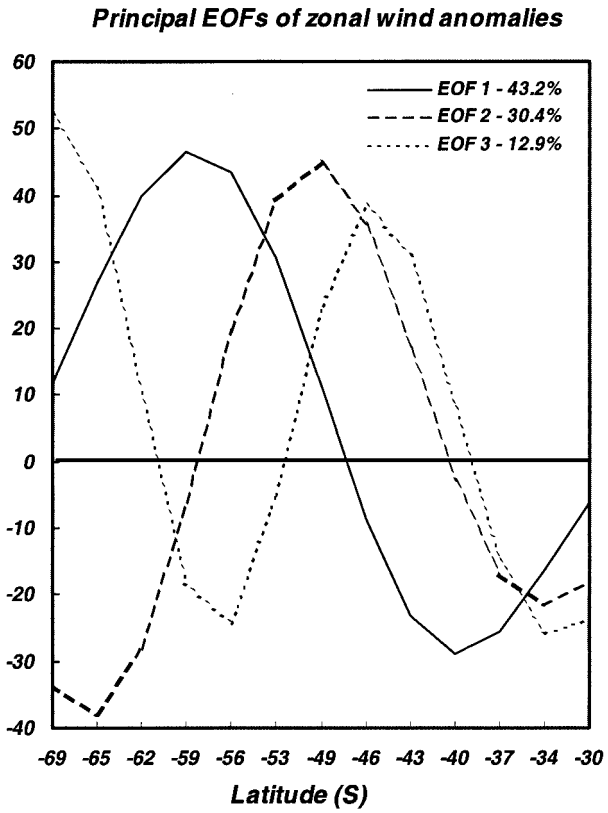

FIG. 1. The three leading EOFs of zonal mean zonal wind anomalies at the 0.5-σ level between 30° and 69°S.

and modeling studies referred to earlier and reveals the equivalent barotropic structure of the oscillation. The largest correlations are found near 40° and 60°S extending through much of the troposphere. The correlations with $[T]$ are generally weaker but are compatible through the thermal wind relationship with the patterns in $[u]$. The correlations with $[u^*v^*]$ peak in the upper troposphere between 40° and 60°S and are very small outside this region. For $[v^*T^*]$ the correlations reach a maximum of 0.25 between 50° and 55°S in the lower troposphere where the anomalous flux is equatorward for positive index values.

Figure 3 shows that contemporaneous correlations underestimate the relationship with $[u^*v^*]$ because the peak flux anomalies precede those in the index. For the 0.5-σ level, at 49°S (where the momentum flux variations are greatest) the correlation coefficient is -0.22 at lag zero, but it reaches -0.48 40 h before the peak in the index. For lags beyond $+1$ day, the correlations are small. As we shall see later, the variations in $[v^*T^*]$ are generally in phase with those in the index.

c. Time variation of the HLM index

A spectral analysis, following Jenkins and Watts (1968), of the 8-hourly index values is shown in Fig. 4. The spectrum has no pronounced peaks but, for periods extending from 3 days through the intraseasonal range, shows significant departures from the red noise spectrum for a first-order Markov process with the same lag-1 autocorrelation (0.991). The autocorrelations indicate that the variance explained by persistence falls to 10% at lags of 14 days and to 1% at lags of 33 days. The spectra of the zonal mean zonal wind anomalies at the peak latitudes 40° and 59°S, and of the eddy momentum flux at 49°S (not shown), are similar to that of the HLM index.

Cross-spectral analysis confirms the lack of any phase lag between the HLM index I and the zonal wind anomalies at all latitudes between 40° and 59°S (apart from the 180° phase reversal near 48°S). The low-frequency portion of the cross spectrum between I and the peak eddy momentum flux anomalies at 49°S are shown in Fig. 5. The coherence lies between 0.6 and 0.8 for periods greater than 8 days. At very low frequencies the phase difference is 180°, and the anomalous momentum flux helps to maintain the zonal wind anomaly against friction. At intermediate frequencies, where the HLM variance peaks, the two series are almost in quadrature. Here the momentum flux variations mainly contribute to the change in index values, but a small component also helps to maintain departures in the index against friction. While the angular momentum anomalies observed by Feldstein (1998) in midlatitudes of the Southern Hemisphere showed evidence of poleward propagation and high-frequency eddies contributed to their development, low-frequency (and cross-frequency) eddies were largely responsible for their decay, in contrast to the result obtained here.

The distribution of the daily values of I (not shown) is very close to normal, with no evidence of skewness in favor of negative or positive departures. A similar result was subsequently obtained for the 60°–40°S zonal index for Australian data presented in Kidson (1988a). Hartmann and Lo's (1998) results from European Centre for Medium-Range Weather Forecasts analyses showed an index distribution that was slightly skewed in favor of negative index values, with low index spells lasting slightly longer than high index events. An even stronger bias toward negative index values was found in Robinson's (1991) two-level model results. There is no evidence either of clustering around preferred states with index values differing from zero. Yoden et al. (1987) have suggested that the transition between the single and double jet regimes is indicative of a bimodal distribution, but the work of Hansen and Sutera (1988), for example, indicates that evidence of bimodality in the Southern Hemisphere is hard to find.

3. Composite analyses

In order to examine variations in the HLM with relevance to climate prediction, detailed analysis has concentrated on four subsets of the data. These include

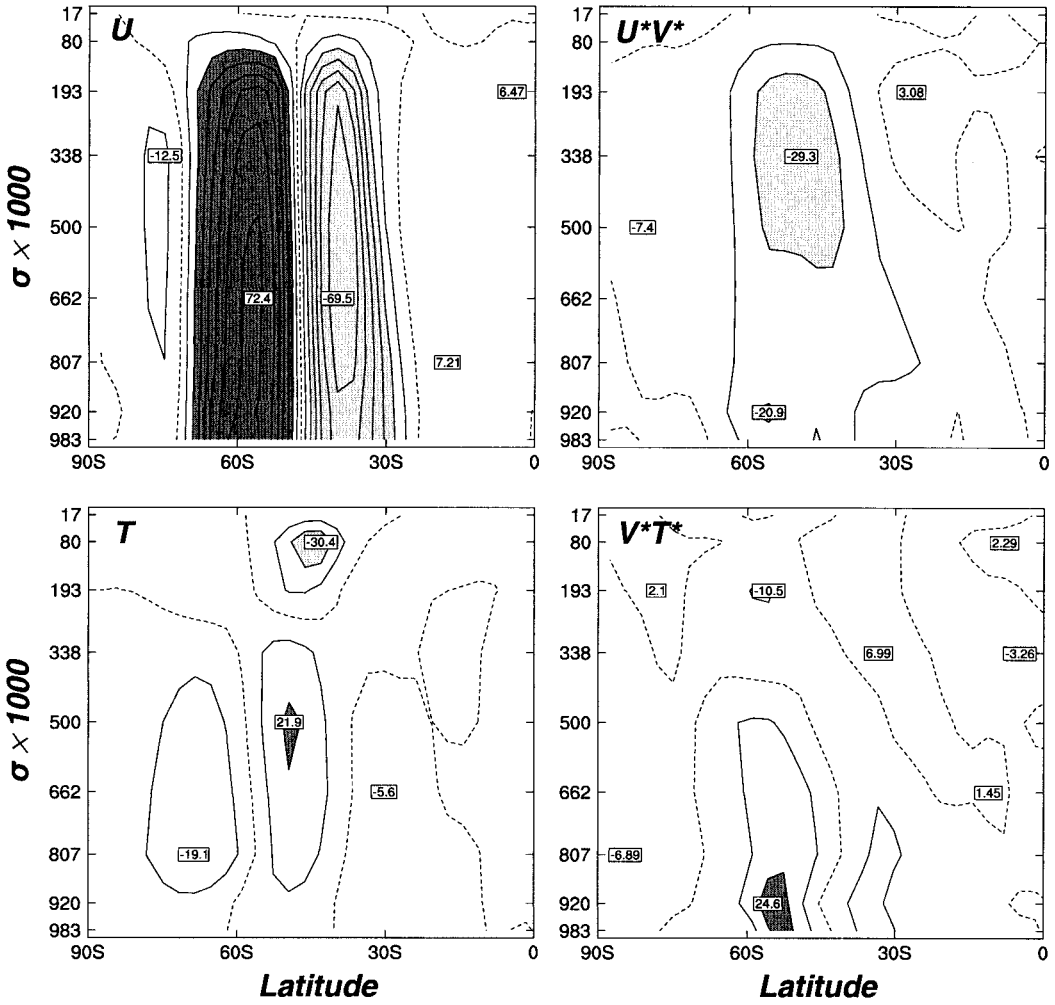

FIG. 2. Correlations of the HLM index with anomalies in the zonal means of the zonal wind u, eddy momentum flux $u^* v^*$, temperature T, and eddy heat flux $v^* T^*$.

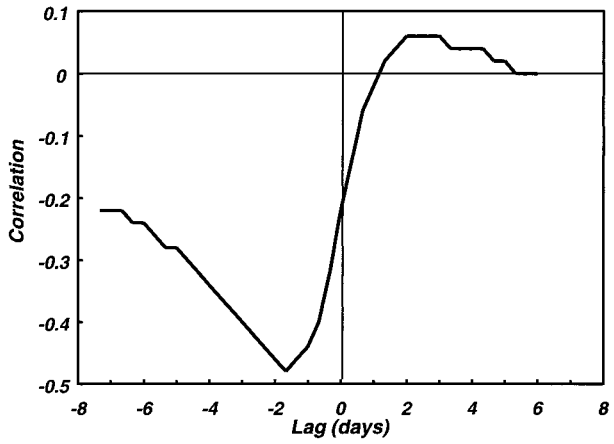

FIG. 3. Lag correlations of the eddy momentum flux $[u^* v^*]$ at 0.5 σ, 49°S with the high-latitude mode.

- transitional periods in which the index I changed from a positive peak exceeding a specified threshold to a negative period of less than the same threshold within a relatively short time frame (class N) and similar transitions in the opposite sense (class P); and
- persistent periods in which the index remained above a particular positive threshold (H) or below the same negative threshold (L) for a sustained period.

The initial and final dates for each period were determined by the time at which the 10-day low-pass-filtered index reached the corresponding peak in the series (for transitional periods), or when it first and last exceeded the threshold for the persistent periods. Because these periods were of variable length, composites were built from three overlapping segments composing time windows centered on the initial and final dates, and on the date halfway between them. They were then merged by deleting an arbitrary number of days from the end of the first segment, the start and end of the

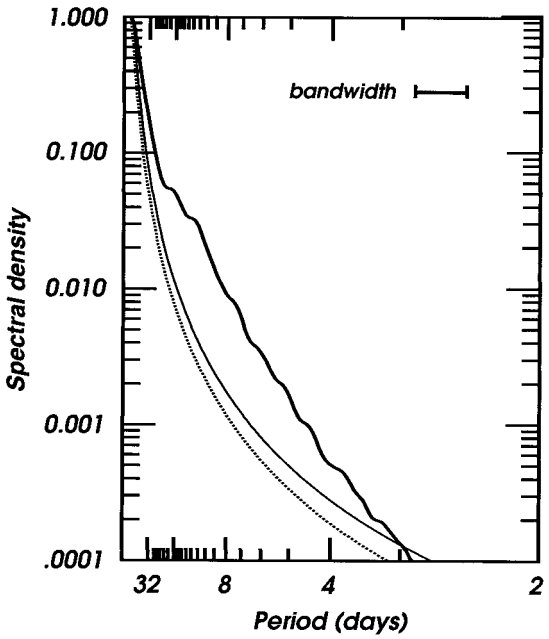

FIG. 4. Spectrum of the HLM index (heavy line). The dotted line represents the spectrum of a red noise process with the same lag-1 autocorrelation, and the thin continuous line the 5% significance level for spectral peaks.

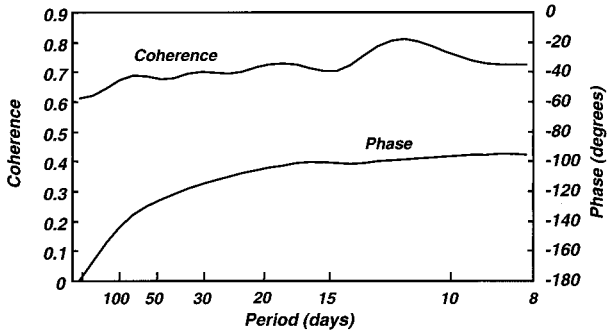

FIG. 5. Coherence and phase between the HLM index and the eddy momentum flux $[u^* v^*]'$ at 49°S.

middle segment, and the start of the last segment so that a smooth transition of index values was achieved across the joins between them. The resulting composites were not particularly sensitive to the location of the join between segments, which are indicated by lines across the time sections displayed in the following figures. A full set of model fields was composited for each of these four classes.

Although the composites were obtained differently, the nomenclature follows that of Yu and Hartmann (1993) with classes H and L covering periods with extreme positive and negative index values, while N and P represent conditions where the index has a strong negative or positive trend, respectively, between two peaks of opposite sign. Their purpose is to identify common characteristics of these four classes rather than compute detailed budgets, where the varying length of each episode needs to be considered. The continuity shown in the following cross sections is taken as an indication of the success of the method.

a. Transitional periods

Transitional periods were selected using a threshold of ± 1 standard deviation of *I*. This provided a set of 28 positive (P) and 38 negative (N) transitions over time intervals ranging between 18 and 89 8-h periods. In order to focus on periods of similar length, where the changes occurred directly, analysis was restricted to the 21 positive and 28 negative transitions where the interval between the opposing peaks was less than 16 days. The mean time between opposing peaks was 13 days for both positive and negative transitions, corresponding to periods on the order of 26 days.

The progression of events during this period is best shown by the time sections of the zonal wind and momentum flux anomalies at the 0.5-σ level in Figs. 6 and 7. In these figures the anomalies are calculated relative to the mean for the composites, which include a full range of index variations. In each case these figures show the parallel growth and decay of zonal wind anomalies surrounding the peaks in the index near 40° and 60°S and, in agreement with cross-spectral analysis, there is no evidence of meridional propagation. This differs from the results reported in the modeling study of James and Dodd (1996), and in the analysis of observed data by Feldstein (1998). The momentum flux anomalies are centered on 50°S, between the bands where the complementary changes in momentum content are occurring. The maximum poleward or equatorward flux anomalies are found as the peak zonal wind anomalies are developing and their amplitude is small at, and immediately after, the zonal wind maxima.

Composite meridional cross sections (not shown) indicate that the amplitude of the maximum eddy covariance $[u^* v^*]$, near the 0.3-σ level, is -33 m^2 s^{-2}. This peak value changes little throughout the cycle, but it moves from 33° to 41°S as the index changes from low to high values (cf. Kidson and Sinclair 1995). The region of equatorward transport near 61°S for low index values virtually disappears for the high index composites. Changes in the eddy momentum flux to the north of 35°S are weak and in the opposite sense to those at 49°S, while changes south of 65°S are also small. In each case, fluxes at high and low latitudes contribute little to the changes in momentum content of the bands centered on 40° and 60°S.

Further insight into the forcing of the zonal wind during these transitional periods is provided by Figs. 8 and 9, which show time sections of the vertical profiles of $[u]'$ at 60°S, $[u^* v^*]'$ at 49°S, and the anomalous eddy heat flux $[v^* T^*]'$ at the 0.81-σ level for the N and P transitional periods. The vertical profile of $[u]'$ at 40°S is similar to that at 60°S and each shows a tendency for

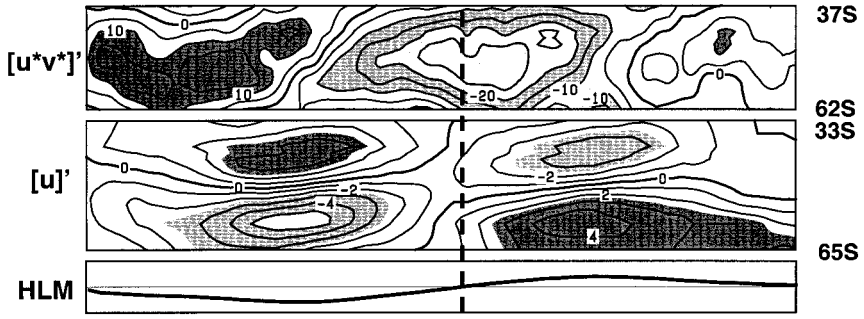

FIG. 6. Time section of zonal mean zonal wind $[u]'$ and eddy momentum flux $[u^* v^*]'$ anomalies for positive index transitions at the 0.5-σ level. The units are m s^{-1} and m^2 s^{-2}, respectively. The composite index values are shown below within a range of ± 2 σ, and the horizontal scale covers approximately 21 days.

the zonal wind anomaly to build quickly at upper levels, following the peak anomaly in eddy momentum transport between the two bands. It then slowly decays while the eddy flux anomalies remain small. Although not as marked in the P transitions at 60°S, there is a tendency for the zonal wind anomaly to decay more quickly at lower levels in response to the surface friction. The eddy heat fluxes are shown for the 0.81-σ level where their changes are largest. In comparison to the eddy momentum fluxes, they are not particularly well organized and the variations about the mean are relatively small. Near 52°S, where the zonal mean heat flux is approximately -16 K m^{-1} s^{-1}, the variations throughout the cycle are typically ± 2 K m^{-1} s^{-1}. The general pattern between 40° and 60°S is for poleward (equatorward) heat flux anomalies to coincide with, and follow, equatorward (poleward) momentum flux anomalies at the same latitude. The poleward heat flux anomalies tend to reinforce the upward component of the Eliassen–Palm (EP) vector at lower levels when the index is negative and the zonal wind is stronger near 40°S. Large variations in the heat flux occur at high latitudes but they do not show a consistent pattern of variation throughout the cycle.

This pattern of increased poleward heat fluxes at midlatitudes for low index values is generally consistent with that observed in atmospheric datasets (Kidson 1988b; Karoly 1990) and also in the model results of Yu and Hartmann (1993). Both Yu and Hartmann (1993) and Feldstein (1998) note that the momentum fluxes peak during the development of the zonal wind anomalies and are followed by peak values of the heat flux departures. For other modeling studies the results are less clear-cut. Feldstein and Lee (1996), for example, found that the maximum heat fluxes occurred before the peak in the zonal winds but their behavior after that depended on the sign of the anomaly. They argued that the occurrence of the peak momentum fluxes prior to the maximum in the eddy heat flux anomalies is not consistent with the pattern of baroclinic growth followed by barotropic decay expected for baroclinic life cycles (Simmons and Hoskins 1978), and suggests that variations in the zonal wind profile do not have a large role in organizing the behavior of the eddies.

b. Persistent periods

Persistent periods were defined as intervals over which the low-pass filtered index remained above (H) or below (L) one standard deviation for periods of 15 days or more. This gave a total of 28 H and 25 L cases with a mean period of 23 days for compositing. Increasing the threshold to 1.5 standard deviations would have reduced the number of cases by a factor of 3–4, while increasing the duration to 20 days would have halved the number of cases available for analysis. The

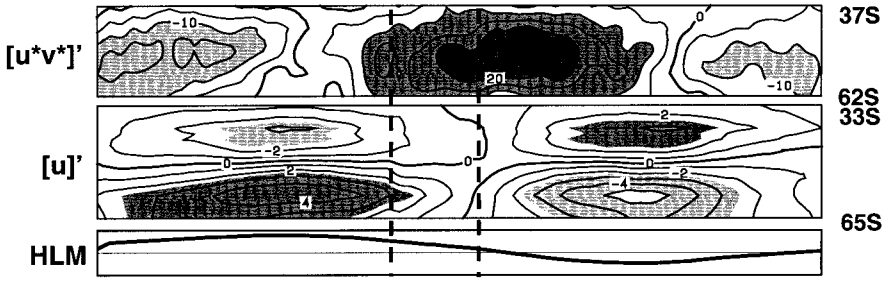

FIG. 7. Time section of zonal mean zonal wind $[u]'$ and eddy momentum flux $[u^* v^*]'$ anomalies for negative index transitions at the 0.5-σ level. The units are m s^{-1} and m^2 s^{-2}, respectively. The composite index values are shown below within a range of ± 2 σ, and the horizontal scale covers approximately 21 days.

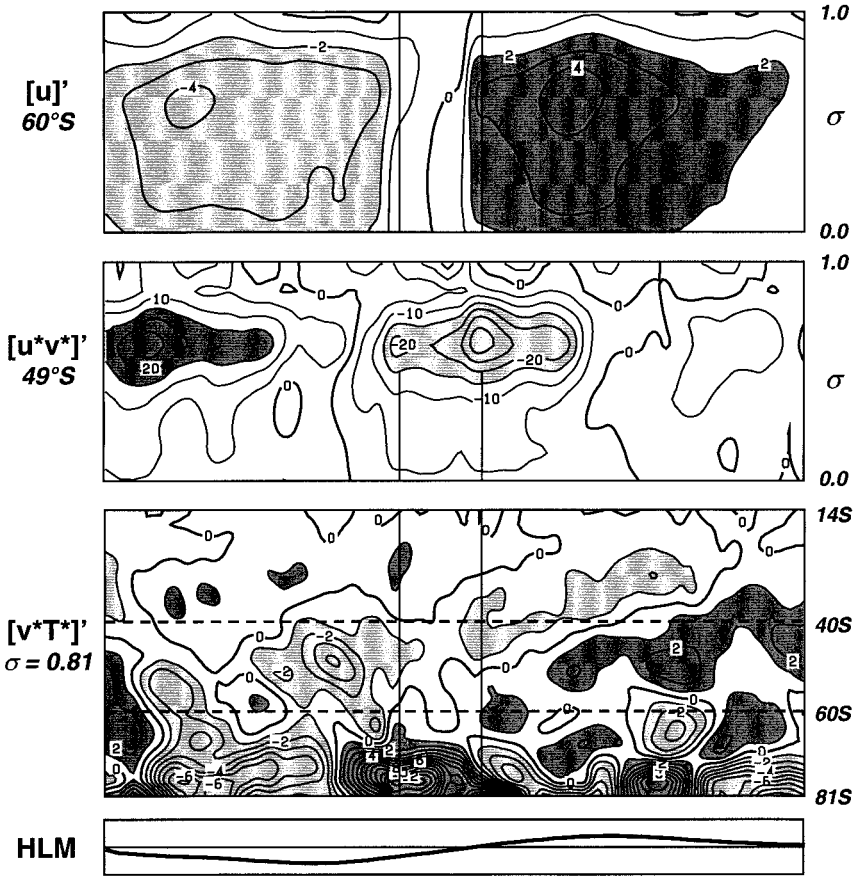

FIG. 8. Time section of zonal mean zonal wind $[u]'$ and eddy momentum flux $[u^* v^*]'$ anomalies for persistent positive spells at the 0.5-σ level. The units are m s^{-1} and m^2 s^{-2}, respectively. The composite index values are shown below within a range of ± 2 σ, and the horizontal scale covers approximately 29 days.

three segments composing the composite were centered on the times where the index first exceeded the threshold, fell below it, and halfway in-between. The window size for each segment was increased over the transitional cases because of the somewhat longer timescale of the persistent episodes.

The characteristic zonal wind and eddy momentum flux anomaly patterns are shown in Figs. 10 and 11. These are again taken relative to the overall means for the composites, which will be biased slightly in favor of the predominant zonal wind or momentum flux departures. The composite mean momentum fluxes in the H cases in Fig. 10, for example, are generally more strongly southward than those for the L cases in Fig. 11. Nevertheless, these figures show increased momentum transports prior to the peak index values and persistence of these fluxes at a weaker level for the duration of the spell. The momentum flux patterns leading up to the positive peak in the index in Fig. 10 are not very different from those prior to the positive peaks in Figs. 6 and 7, although their overall magnitude is somewhat larger. The tendency of the index after the peak value is reached depends on the subsequent behavior of the momentum flux.

c. Variations in surface cyclone activity

Estimates of surface cyclone activity are available from the location and tracking scheme described by Sinclair (1994, 1995), which has now been applied to validation of the CSIRO9 model (Sinclair and Watterson 1999). Vorticity centers have been identified at the 100-hPa level and, where appropriate, successive locations at 8-h intervals have been formed into tracks. Composites of the total number of vorticity centers between 43° and 56°S, and the number of new centers appearing at each analysis time are shown in Fig. 12 for the transitional periods described above. Both series follow similar patterns, although there is more day-to-day variability in the smaller numbers of new centers observed. The factor of 9 between values in the two series implies a mean lifetime of around 3 days for each system. With the exception of the first (+) peak in the negative index transitions, the peak cyclone activity occurs prior to the

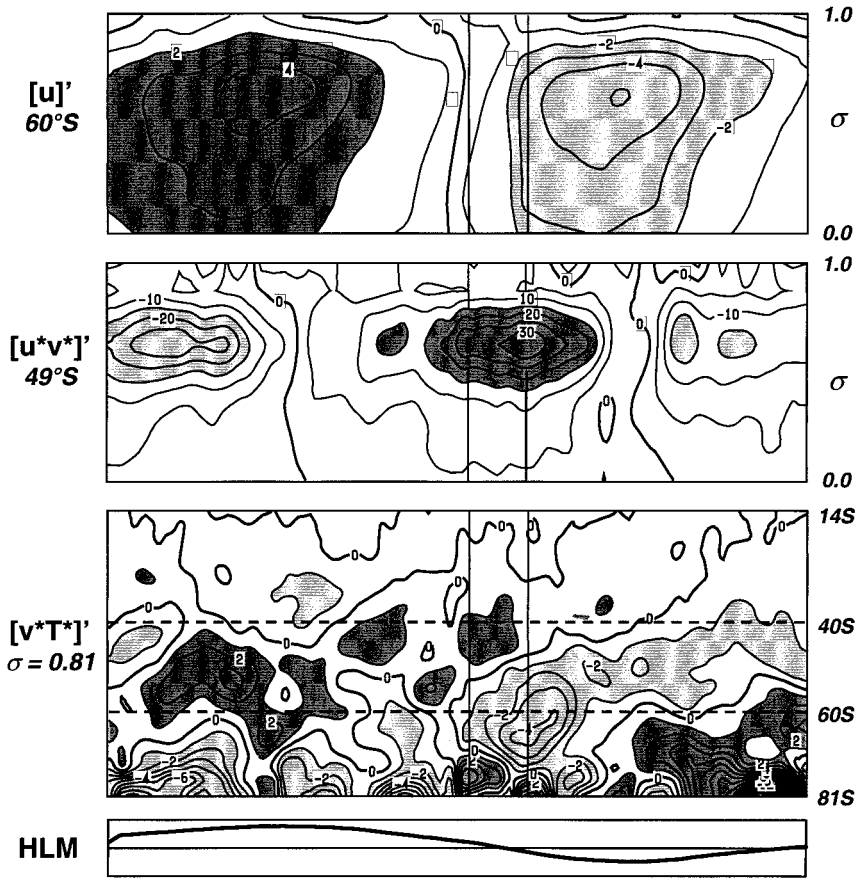

FIG. 9. Time section of zonal mean zonal wind $[u]'$ and eddy momentum flux $[u^* v^*]'$ anomalies for persistent negative spells at the 0.5-σ level. The units are m s^{-1} and m^2 s^{-2}, respectively. The composite index values are shown below within a range of ± 2 σ, and the horizontal scale covers approximately 33 days.

extremes of the index and the zonal wind departures. On average the lead is around three 8-h periods, which may be compared with the 40-h lead for which the best correlation was obtained between the momentum transport at 49°S and the HLM index.

d. EP fluxes

The overall patterns of Eliassen–Palm fluxes (Edmon et al. 1980) are similar in each phase of the index and in general agreement with those previously reported (e.g., Karoly 1990; Yu and Hartmann 1993). They show a strong upward component in low levels related to the eddy heat transport and a weaker equatorward component at upper levels in the troposphere due to the eddy momentum fluxes. The variations with the phase of the HLM index are revealed more clearly by the differences between the H and L, and P and N phases in Fig. 13. In this figure, the H composite includes 17 8-h periods around the second peak in Fig. 6 and the first peak in

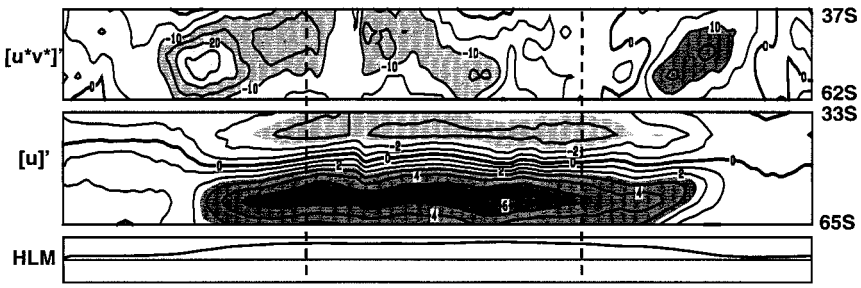

FIG. 10. Composites of the zonal wind anomalies at 60°S, eddy momentum flux anomalies at 49°S, and the eddy heat flux anomalies at the 0.81-σ level for positive index transitions. The units are m s^{-1}, m^2 s^{-2}, and K m s^{-1}, respectively.

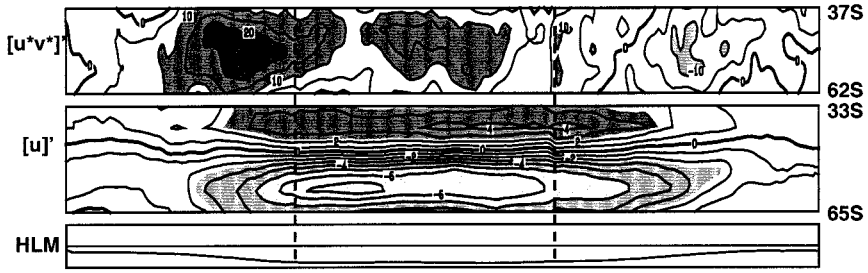

FIG. 11. Composites of the zonal wind anomalies at 60°S, eddy momentum flux anomalies at 49°S, and the eddy heat flux anomalies at the 0.81-σ level for negative index transitions. The units are m s^{-1}, m^2 s^{-2}, and K m s^{-1}, respectively.

Fig. 7. The opposite combination was taken for the L composite and in each case they are representative of index values of exceeding ± 1 standard deviation. The P and N composites were obtained from 17 consecutive 8-h states in the centers of Figs. 6 and 7, respectively. The divergence field is the forcing for $\cos\theta\partial u/\partial t$ as in Yu and Hartmann (1993), and the shading reflects its calculation in finite difference form. We have assumed

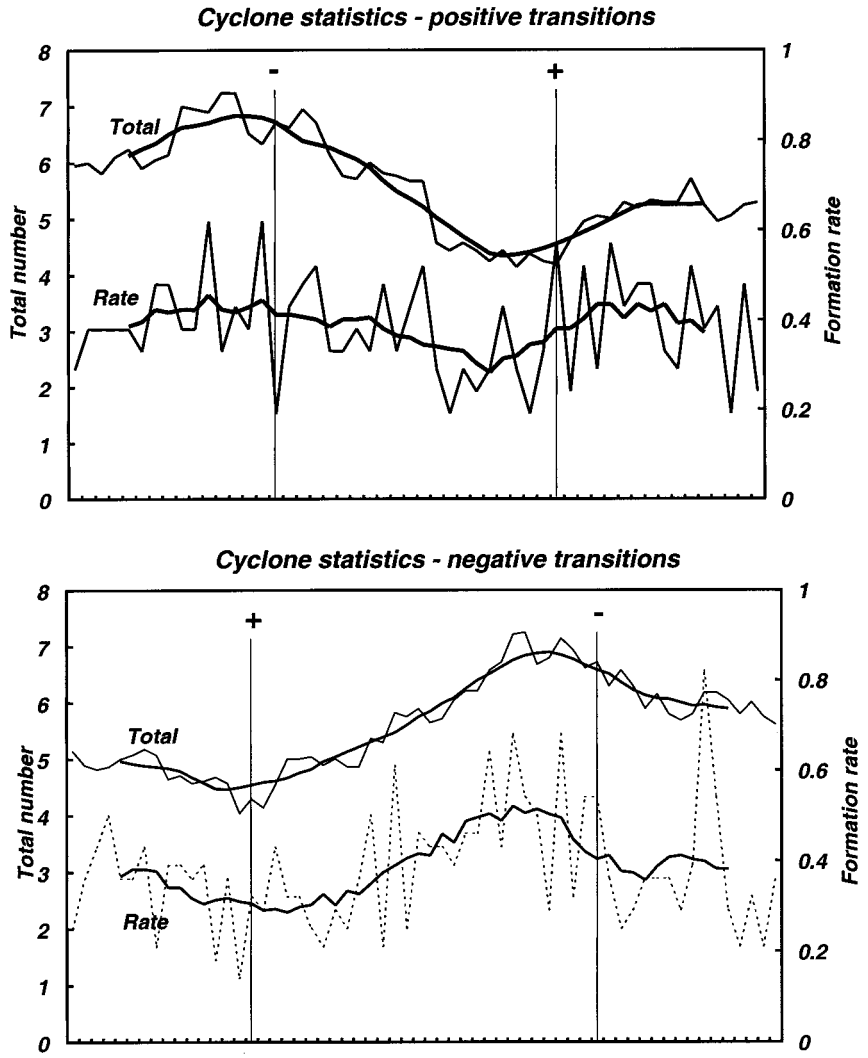

FIG. 12. Time series of the number of 1000-hPa vorticity centers and the rate of formation of new centers (per 8-h period) between 43° and 56°S for the transitional periods composited in Figs. 6 and 7. The vertical lines indicate the time of the + and − peaks in the index values, and the tick marks on the horizontal axis indicate 8-h time units. The heavy line through each data series is the 3-day running mean.

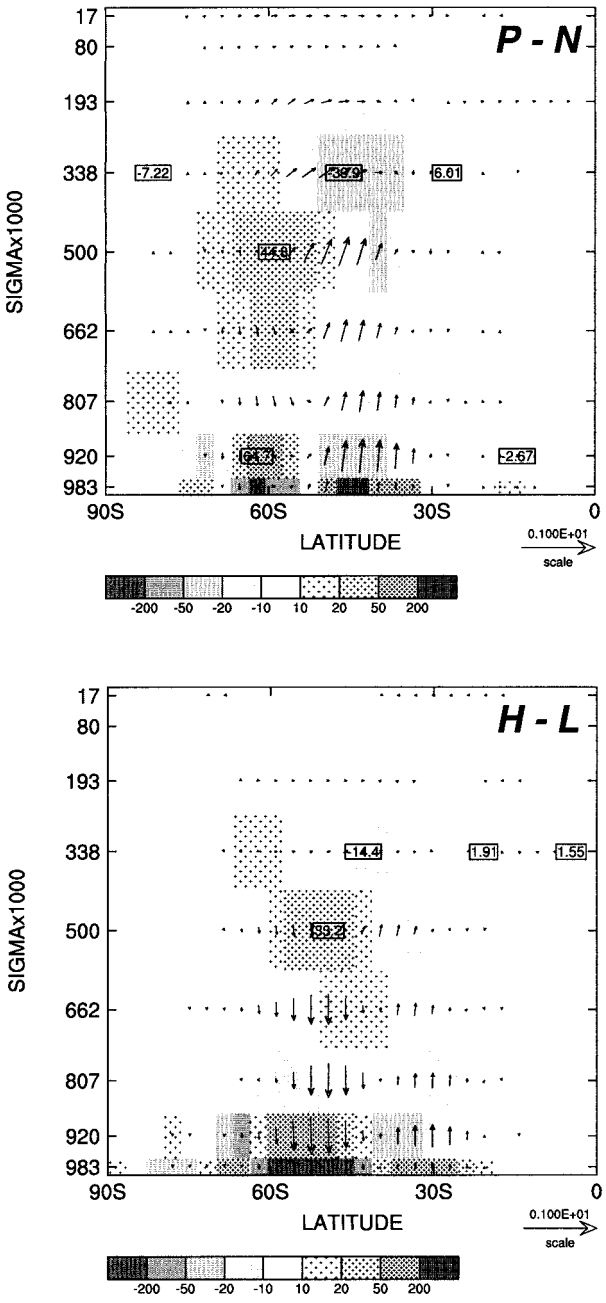

FIG. 13. Differences in the EP flux between H and L, and P and N phases of the high-latitude mode. The vectors are plotted as in Edmon et al. (1980), with a unit length of 10^{15} m^3 in the horizontal and 63.7 m^3 kPa in the vertical. The units for the divergence are 10^{-6} m s^{-2}.

that $[v^*T^*]$ is zero at the upper and lower boundaries, to ensure that the vertical integral of Yu and Hartmann's baroclinic term is zero. This leads to large divergences in the thin bottom layer but otherwise the pattern is similar to the sum of their barotropic and baroclinic terms.

The differences are clearer in the P–N pattern where the sign of the eddy forcing changes around 50°S to produce the appropriate acceleration in the zonal wind. The H–L pattern is closer to Karoly's (1990, Fig. 6) MIN–MAX difference at middle and upper levels in the troposphere with the maximum convergence sloping poleward with increasing height. The low-level convergence is generally in the sense of maintaining the anomalous zonal flow against increased or reduced friction, but the H–L difference is not particularly well aligned with the latitudes where the largest anomalies occur (see Fig. 2).

e. Momentum budget analysis

A more comprehensive picture of the response of the zonal index to changes in the momentum forcing is provided through momentum budget calculations. In view of the barotropic nature of the HLM we have simplified this analysis by taking vertical integrals of the zonally averaged equation (e.g., Newell et al. 1972):

$$\frac{\partial [M]}{\partial t} + \frac{1}{a\cos\phi}\frac{\partial}{\partial \phi}[J_\phi]\cos\phi + \frac{\partial}{\partial p}[J_p] = -\left[\frac{\partial \Phi}{\partial \lambda}\right], \quad (1)$$

where

$$M = (\Omega a\cos\phi + u)a\cos\phi \quad (2)$$

$$[J_\phi] = \Omega a^2\cos^2\phi[v] + a\cos\phi([u][v] + [u^*v^*]) \quad (3)$$

$$[J_p] = \Omega a^2\cos^2\phi[\omega] + a\cos\phi([u][\omega] + [u^*\omega^*]) + ga\cos\phi[\tau]; \quad (4)$$

u, v, and ω are the velocity components in pressure coordinates; a is the radius of the earth; Ω its angular velocity; g the acceleration due to gravity; ϕ the latitude; and λ the longitude. Integration of Eq. (1) vertically and between latitudes ϕ_1 and ϕ_2 results in the equation of the form

$$\frac{\partial}{\partial t}\int M\,dm + \frac{2\pi a}{g}\int \{J_\phi(\phi_2)\cos\phi_2 - J_\phi(\phi_1)\cos\phi_1\}\,dp + R = 0, \quad (5)$$

where $dm = a^2\cos\phi\,d\lambda\,d\phi\,dp/g$ and R is a residual term expressing the effects of surface friction and the mountain torque term involving $\partial\phi/\partial\lambda$ in Eq. (1). We make the common assumption that the change of atmospheric mass within the latitude belt leads to insignificant changes in the angular momentum content so that the terms involving Ω disappear from the definition of M and J_ϕ in Eqs. (2) and (4). Separating the term involving the correlation of the zonal mean from the eddies in Eq. (5), we have an equation expressing the balance of angular momentum of the form

$$\frac{\partial M_u}{\partial t} + (F_{m1} - F_{m2}) + (F_{e1} - F_{e2}) + D = 0, \quad (6)$$

where M_u represents the angular momentum relative to

solid body rotation between latitudes ϕ_1 and ϕ_2; F_m and F_e are the mean and eddy fluxes, respectively, across the southern and northern walls; and D is a residual that represents dissipation from the combined surface and mountain torques.

For each of the transitional and persistent composites described above, the momentum budget (6) was analyzed for two latitude belts centered on the opposing angular momentum changes. The northern belt included the volume between rows 20 and 13 of the grid (latitudes 27.1°–49.4°S) while the southern belt extended between rows 7 and 13 (49.4°–68.5°S). The overall change in angular momentum content within the southern latitude belt is approximately 70% of the change within the northern belt.

The results for each composite for the northern belt are shown in Fig. 14. In each case the tendency in momentum content, $\partial M/\partial t$, closely parallels the eddy flux divergence term. Both are positive when index values are decreasing and negative when the index values increase and more momentum is being transported southward at the southern boundary. The contribution of the mean motion term is negligible. The residual term, which largely expresses the surface torque, varies slowly in phase with the index and composites of individual points in the four figures show an approximately linear relationship across the entire range of index values. Low index values imply a stronger zonal flow in the northern band and a greater frictional torque at the surface. The patterns for the southern band (not shown) are generally similar but in the opposite sense from the corresponding patterns in Fig. 14. The amplitude of the momentum content variations is smaller and the total angular momentum is not conserved over the total area of the two bands.

The results are summarized in Table 1, except for the small and nearly constant contribution from the mean meridional circulation, F_m. The flux divergence anomalies required to maintain peak departures of the index against friction are obtained by differencing the values at the centers of the H and L composites to give ± 7 units[1] in each band. Peak flux divergences in the acceleration phase are obtained from differencing the N and P cases, and are nearly twice as large in the range ± 14–16 units. The overall range of the eddy flux divergence for the northern band from Fig. 14 is -3 to $+43$ units, while for the southern band the lower and upper bounds are -6 and $+29$ units. These values are found where the index is high and increasing or low and decreasing.

4. A simple model of the HLM index

In order to evaluate whether a realistic combination of high-frequency stochastic forcing and linear damping can successfully reproduce the observed index variations, we have constructed a simple model of the vertically integrated momentum budget. A similar model has been used by Robinson (1991, 1994) and it is consistent with our analysis of the momentum budget for individual bands in the preceding section.

The departures in angular momentum content of the band, M, change in response to time-dependent forcing $F(t)$ and linear damping as shown in Eq. (7):

$$\frac{\partial M}{\partial t} + cM - F(t) = 0, \tag{7}$$

where c is a constant that, in the absence of zonal-eddy feedback, represents linear frictional damping with timescale $\tau = 1/c$. Formally, however, it may also include zonal-eddy feedbacks proportional to M (Robinson 1994).

The eddy forcing $F(t)$ has been prescribed in the simple Markov form

$$F(t + 1) = aF(t) + b(t), \tag{8}$$

where a specifies the lag-1 autocorrelation, and $b(t)$ is a random normally distributed value with a mean of zero and standard deviation of $(1 - a^2)^{1/2}$. As the observed autocorrelation of the eddy momentum transports at lag n falls off somewhat faster than r_1^n, we have chosen a to be 0.774, the cube root of the lag correlation of 0.464 at 1 day observed for $[u^*v^*]$ at 0.5 σ, 49°S.

In finite difference form, with a forward time step, Eq. (7) becomes

$$M(t + 1) = pM(t) + q\{F(t + 1) + F(t)\},$$

where

$$p = (1 - c\delta t/2)/(1 + c\delta t/2) \qquad q = \delta t/(2 + c\delta t).$$

Here we scale $\delta t = 1.0$ (corresponding to the 8-h interval between analyses) and determine c iteratively to give an appropriate balance between the magnitudes of the eddy forcing and friction terms. The magnitude of c also determines the standard deviation and the autocorrelation of M.

The autocorrelation of M is compared with that for the HLM index in Fig. 15 for $c = 0.07$ and $c = 0.035$ and a held constant at 0.774. A good match is obtained over the first 2–3 days with $c = 0.07$ with the 1-day lag correlation for M of 0.943 matching that of the HLM index I, but there is insufficient persistence after 5 days. Better agreement at longer lags is obtained by halving the value of c to 0.035, but the overall shape of the response is somewhat unsatisfactory. Another measure of the performance of the model has been comparison of the relative magnitudes of dM/dt and the eddy and frictional forcing, through their standard deviations. From Table 1 we would expect the ratio of the friction to the eddy forcing to be around 0.4 and 0.5 in the northern and southern latitude belts, while the ratio of eddy forcing to dM/dt should be 1.2 and 1.4, respectively. With $c = 0.07$, we obtain 0.49 for the cM/F ratio

[1] Note: 1 unit is 10^{18} kg m^2 s^{-2}.

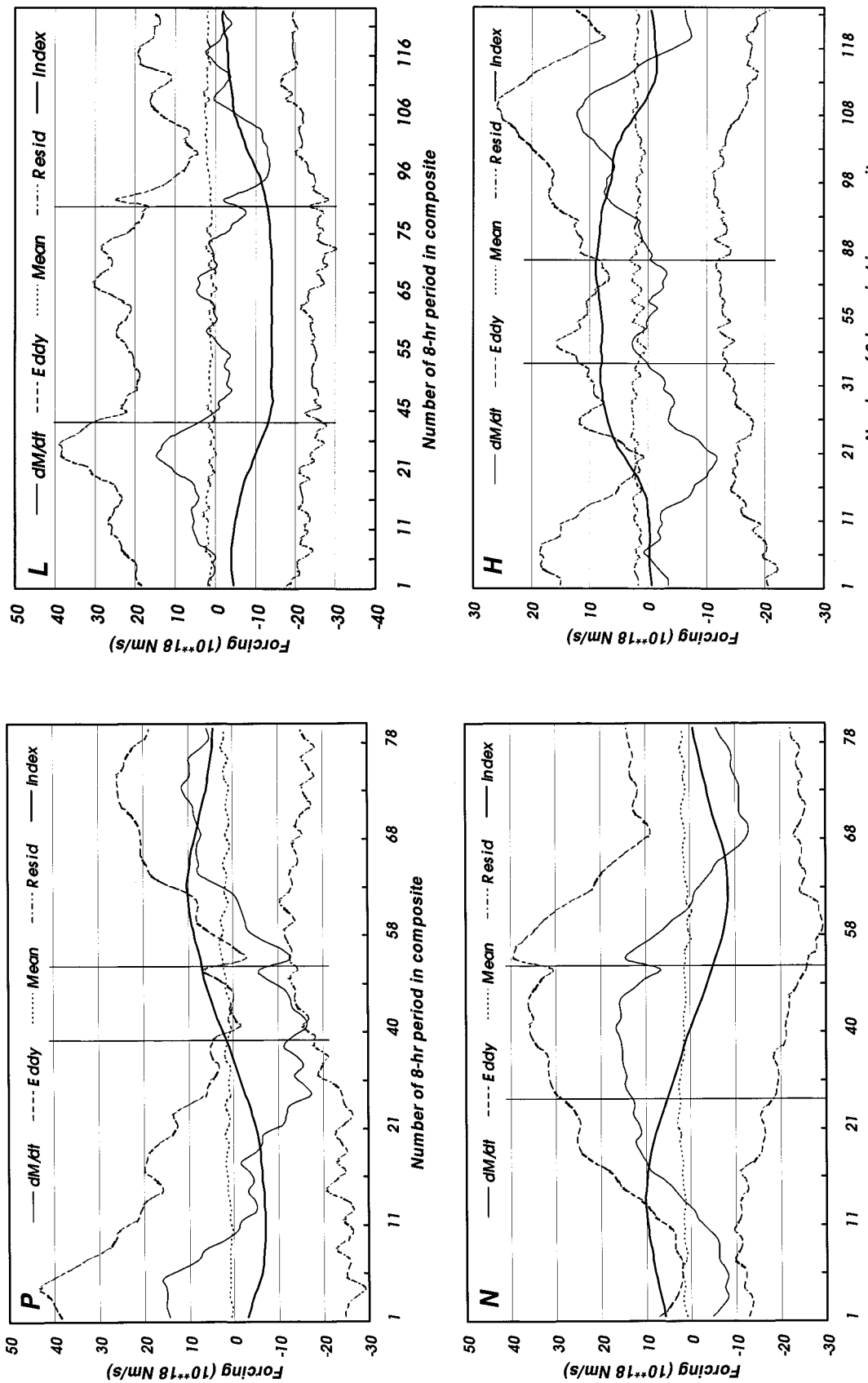

FIG. 14. Time sections of vertical integrals of relative angular momentum content, the net mean and eddy transport of angular momentum, and the residual term, together with the HLM index, for composites P (upper left), N (lower left), L (upper right), and H (lower right). The units of the momentum budget terms are 10^{18} N m s^{-1}.

TABLE 1. Amplitude of momentum tendency (dM/dt), eddy forcing (Fe), and friction (Fr) terms during the H, L, P, and N phases of the HLM for bands centered on 40° and 60°S. The units are 10^{18} N m s^{-2}.

	Phase	H	L	P	N	(H–L)/2	(P–N)/2
Northern band	dM/dt	0	0	−12	14	0	−13
	Fe	10	24	2	34	−7	−16
	Fr	−13	−25	−15	−22	6	4
Southern band	dM/dt	0	0	9	−10	0	10
	Fe	18	4	27	−1	7	14
	Fr	−17	−3	−16	−8	−7	−4

and 1.15 for $F/(dm/dt)$. For $c = 0.035$ the cM/F ratio is 0.37, which is close to the observed range, but the $F/(dm/dt)$ ratio of 1.08 is less realistic.

For additional low-frequency feedbacks proportional to M, or high-frequency contributions proportional to dM/dt (see Robinson 1994), the form of Eq. (7) will remain the same and the lag correlation patterns that result from it will have similar shapes. A better fit to the observed autocorrelation of I is apparently possible only by including forcing terms with greater persistence. From the momentum budgets of the previous section, we obtain peak momentum content anomalies of around $\pm 3.3 \times 10^{24}$ m^{-2} s^{-1} and the corresponding anomalies in the frictional torque are approximately $\pm 7 \times 10^{18}$ m^2 s^{-2}. This gives a relaxation time on the order of 5 days, corresponding to $c = 0.067$. Positive zonal → eddy feedback, with about half the amplitude of the friction term, would effectively lower the value of c to 0.035 and provide a more realistic response at lower frequencies.

5. Discussion and conclusions

Our analysis shows that the CSIRO9 model has an equivalent barotropic pattern of variation in the zonal mean wind, similar to that observed previously in the atmosphere and in a range of numerical models. This mode is characterized by opposing variations in the angular momentum of belts centered near 40° and 60°S, which are largely forced by changes in the strength of the eddy momentum flux near 50°S. Neither composites for transitional and persistent periods nor spectral analysis show evidence for meridional propagation of the zonal wind anomalies.

The 8-h time resolution in the data series has enabled us to show that both upper-level momentum flux and surface cyclone frequency anomalies peak prior to maxima in the zonal wind. The zonal wind anomalies develop relatively quickly at all levels, but appear to decay more slowly in the upper troposphere. The eddy heat fluxes are generally less well organized than the mo-

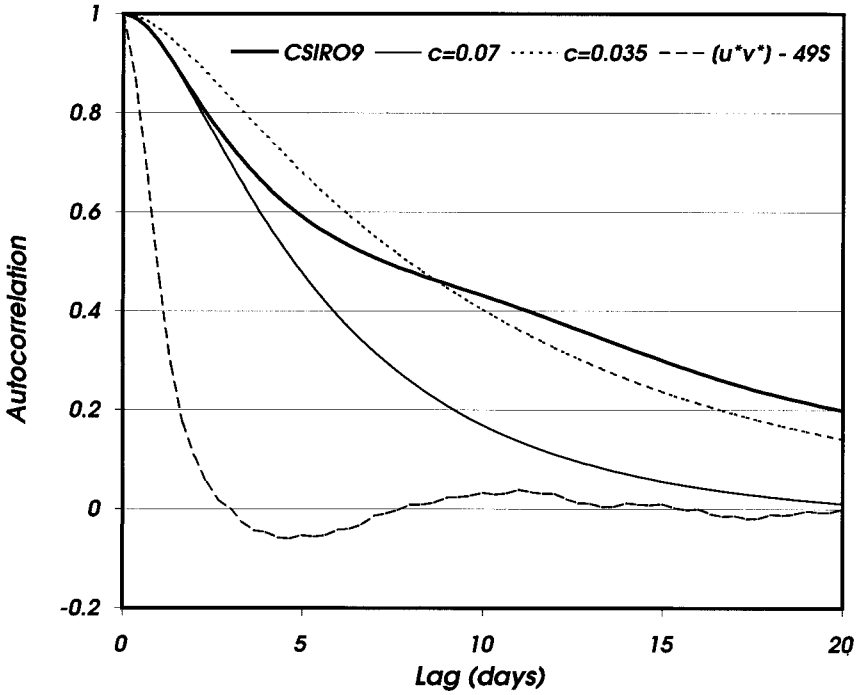

FIG. 15. Autocorrelations of the HLM index, and its simulation in response to random eddy forcing. Also shown are the lag correlations of the eddy momentum flux at 49°S and of the total momentum transport in individual eddies at the 0.5-σ level.

mentum flux variations. They tend to be in phase with the zonal wind departures and contribute to the maintenance of the anomalous low-level flow against friction, as do low-frequency variations in the momentum flux.

Momentum budget analysis for bands centered on the maxima in the zonal wind departures shows that variations in the acceleration of the zonal wind are closely paralleled by those in the eddy momentum flux convergence. The contribution from the mean meridional circulation is small and surface friction, which varies almost linearly with the anomalous momentum content of the band, completes the balance. Eddy momentum flux anomalies are approximately twice as strong during the acceleration phase as those required to maintain peak zonal wind anomalies against friction.

A simple model of the vacillation provided a reasonable approximation to the behavior of the zonal index from stochastic forcing with the comparatively short timescale observed in the momentum flux at 49°S. This was achieved with a realistic balance between the three principal terms in the vertically integrated momentum budget: the acceleration of the zonal wind; eddy forcing; and a residual term including friction and zonal → eddy feedbacks. Where the zonal → eddy feedback was small, an excellent fit was obtained to the observed autocorrelation of the zonal index out to lags of 3–4 days. For an acceptable low-frequency response, a smaller drag coefficient was required. This could be achieved through positive zonal → eddy feedback of about one-half the amplitude of the friction term, but at the expense of a less realistic high-frequency response.

The atmospheric results from Hartmann and Lo (1998) show that the high-latitude mode is largely independent of the zonal wind profile and its variations throughout the year. This implies a fairly robust mechanism, which is insensitive to variations in the zonal flow in both time and space. Within the CSIRO9 model we see behavior similar to that described by Feldstein and Lee (1996) with peaks in the zonal index resulting from impulsive eddy forcing of stochastic origin, followed by a period of slow decay induced by friction at the lower boundary. At low frequencies the acceleration of the zonal wind is small and an approximate balance is maintained between the eddy forcing and frictional dissipation. For intraseasonal variations the acceleration term is about twice the size of the friction term and, as the spectral analysis shows, the eddy momentum transports and index variations are largely in quadrature.

This is consistent with the simple model results in section 4, which suggest that positive feedback is needed only for adequate response at lower frequencies. Indeed, the lag correlations shown in Fig. 3 for the complete dataset indicate that, on shorter timescales, momentum fluxes are only slightly influenced by the preceding values of the index. Large and increasing index values, for example, may either increase further or change sign, as shown in the N and H composites. We have not found any evidence for marked changes in eddy behavior related to changes in the zonal wind shear as reported, for example, in the simpler models of Akahori and Yoden (1997) and Hartmann and Zuercher (1998).

While the results of this model-based study may not apply in their entirety to the Southern Hemisphere circulation, the prospects for predicting this important mode of intraseasonal variability appear bleak and we have not commented on them earlier. We attempted regression-based forecasts of the HLM index but achieved only slight improvements over the Markov decay at intervals of a few days, by inclusion of momentum flux as a predictor. Cluster analysis of time series of index and momentum flux values also failed to identify any initial states from which it was possible to improve on persistence. It will be of interest to see whether ensemble forecasts show skill in predicting the zonal index. While detailed forecasts of its behavior may be impossible, there remains the possibility that variations in surface properties (SST, sea ice) may favor the prevalence of one phase or another. We have detected some influence of sea temperature variations at longer timescales and these will be explored in a separate paper (Watterson 2000).

Acknowledgments. This research was funded in part by Contract CO1628 from the New Zealand Foundation for Research, Science, and Technology. We thank Dr. Mark Sinclair for providing the surface cyclone composites, and Kevin Walsh and David Karoly for their comments on an earlier draft of the manuscript. Revision of the manuscript has been assisted by helpful comments from the reviewers.

REFERENCES

Akahori, K., and S. Yoden, 1997: Zonal flow vacillation and bimodality of baroclinic eddy life cycles in a simple global circulation model. *J. Atmos. Sci.,* **54,** 2349–2361.

Edmon, J. H., B. J. Hoskins, and M. E. McIntyre, 1980: Eliassen–Palm cross sections for the troposphere. *J. Atmos. Sci.,* **37,** 2600–2616.

Feldstein, S. B., 1995: The relationship between inter-annual and intra-annual variability in atmospheric angular momentum in a GCM with climatological SSTs. *Tellus,* **47A,** 240–258.

——, 1998: An observational study of the intraseasonal poleward propagation of zonal mean flow anomalies. *J. Atmos. Sci.,* **55,** 2516–2529.

——, and S. Lee, 1996: Mechanisms of zonal index variability in an aquaplanet GCM. *J. Atmos. Sci.,* **53,** 3541–3555.

Hansen, A. R, and A. Sutera, 1988: Planetary wave amplitude bimodality in the Southern Hemisphere. *J. Atmos. Sci.,* **45,** 3771–3783.

Hartmann, D. L., 1995: A PV view of the zonal flow vacillation. *J. Atmos. Sci.,* **52,** 2561–2576.

——, and F. Lo, 1998: Wave-driven zonal flow vacillation in the Southern Hemisphere. *J. Atmos. Sci.,* **55,** 1303–1315.

——, and P. Zuercher, 1998: Response of baroclinic lifecycles to barotropic shear. *J. Atmos. Sci.,* **55,** 297–313.

James, I. N., and J. P. Dodd, 1996: A mechanism for the low-frequency variability of the mid-latitude troposphere. *Quart. J. Roy. Meteor. Soc.,* **122,** 1197–1210.

Jenkins, G. M., and D. G. Watts, 1968: *Spectral Analysis and its Applications.* Holden Day, 523 pp.

Kalnay, E., and Coauthors, 1996: The NCEP/NCAR 40-year reanalysis project. *Bull. Amer. Meteor. Soc.,* **77,** 437–471.

Karoly, D. J., 1990: The role of transient eddies in low-frequency zonal variations of the Southern Hemisphere circulation. *Tellus,* **42A,** 41–50.

Kidson, J. W., 1988a: Indices of the Southern Hemisphere zonal wind. *J. Climate,* **1,** 183–194.

——, 1988b: Interannual variations in the Southern Hemisphere circulation. *J. Climate,* **1,** 1177–1198.

——, 1991: Intraseasonal variations in the Southern Hemisphere circulation. *J. Climate,* **4,** 939–953.

——, and M. R. Sinclair, 1995: The influence of persistent anomalies on Southern Hemisphere storm tracks. *J. Climate,* **8,** 1938–1950.

Lee, S., and S. Feldstein, 1996: Mechanism of zonal index evolution in a two-layer model. *J. Atmos. Sci.,* **53,** 2232–2246.

Mullan, A. B., and B. J. McAvaney, 1995: Validation of high latitude tropospheric circulation in the Southern Hemisphere (Subproject 9). *Proc. First Int. AMIP Scientific Conf.,* WCRP-92, TD 732, Monterey, CA, WMO, 205–210.

Newell, R. E., J. W. Kidson, D. G. Vincent, and G. J. Boer, 1972: *The General Circulation of the Tropical Atmosphere and Interactions with Extratropical Latitudes.* Vol. 1. The MIT Press, 258 pp.

Nigam, S., 1990: On the structure of variability of the observed tropospheric and stratospheric zonal mean wind. *J. Atmos. Sci.,* **47,** 1799–1813.

Robinson, W. A., 1991: The dynamics of the zonal index in a simple model of the atmosphere. *Tellus,* **43A,** 295–305.

——, 1994: Eddy feedbacks on the zonal index and eddy–zonal flow interactions induced by zonal flow transience. *J. Atmos. Sci.,* **51,** 2553–2562.

——, 1996: Does the eddy feedback sustain variability in the zonal index? *J. Atmos. Sci.,* **53,** 3556–3569.

——, and J. Qin, 1992: Predictability of the zonal index in a global model. *Tellus,* **44A,** 331–338.

Rogers, J. C., and H. van Loon, 1982: Spatial variability of sea level pressures and 500 mb height anomalies over the Southern Hemisphere. *Mon. Wea. Rev.,* **110,** 1375–1392.

Simmons, A. J., and B. J. Hoskins, 1978: The life cycles of some nonlinear baroclinic waves. *J. Atmos. Sci.,* **35,** 414–432.

Sinclair, M. R., 1994: An objective cyclone climatology for the Southern Hemisphere. *Mon. Wea. Rev.,* **122,** 2239–2256.

——, 1995: A climatology of cyclogenesis for the Southern Hemisphere. *Mon. Wea. Rev.,* **123,** 1601–1619.

——, and I. G. Watterson, 1999: Objective assessment of extratropical weather systems in simulated climates. *J. Climate,* in press.

——, J. A. Renwick, and J. W. Kidson, 1997: Low-frequency variability of Southern Hemisphere sea level pressure and weather system activity. *Mon. Wea. Rev.,* **125,** 2531–2543.

Trenberth, K. E., 1979: Interannual variability of the 500 mb zonal mean flow in the Southern Hemisphere. *Mon. Wea. Rev.,* **107,** 1515–1524.

Watterson, I. G., 2000: Southern midlatitude zonal wind vacillation and its interaction with the ocean in GCM simulations. *J. Climate,* in press.

——, S. P. O'Farrell, and M. R. Dix, 1997: Energy and water transport in climates simulated by a general circulation model that includes dynamic sea ice. *J. Geophys. Res.,* **102**, 11 027–11 037.

Yoden, S., M. Shiotani, and I. Hirota, 1987: Multiple planetary flow regimes in the southern hemisphere. *J. Meteor. Soc. Japan,* **65,** 571–585.

Yu, J.-Y., and D. L. Hartmann, 1993: Zonal flow vacillation and eddy forcing in a simple GCM of the atmosphere. *J. Atmos. Sci.,* **50,** 3244–3259.

Zwiers, F. W., 1987: A potential predictability study conducted with an atmospheric general circulation model. *Mon. Wea. Rev.,* **115,** 2957–2974.